

An Energy-Efficient FPGA-based Deconvolutional Neural Networks Accelerator for Single Image Super-Resolution

Jung-Woo Chang, Keon-Woo Kang, and Suk-Ju Kang, *Member, IEEE*

Abstract—Convolutional neural networks (CNNs) demonstrate excellent performance as compared to conventional machine learning algorithms in various computer vision applications. In recent years, FPGA-based CNN accelerators have been proposed for optimizing performance and power efficiency. Most accelerators are designed for object detection and recognition algorithms that are performed on low-resolution (LR) images. However, image super-resolution (SR) cannot be implemented in real time based on the typical accelerator because of the long execution cycles required to generate high-resolution (HR) images, such as those used in ultra-high-definition (UHD) systems. In this paper, we propose a novel CNN accelerator with efficient parallelization methods for SR applications. First, we propose a new methodology for optimizing the deconvolutional neural networks (DCNNs) used for increasing feature maps, based on trained filters. Second, we propose a novel method to optimize the CNN dataflow using on-chip memory so that the SR algorithm can be driven at low power in display applications. Third, we propose a two-stage quantization algorithm to determine the optimized hardware size for a limited number of DSPs. Finally, we present an energy-efficient architecture for SR and validate our architecture on a mobile panel with quad-high-definition (QHD) resolution. Our experimental results show that, with the same hardware resources, the proposed DCNN accelerator achieves a throughput up to 108 times greater than that of the conventional DCNN accelerator. In addition, our SR system achieves an energy efficiency of 92.7 *GOPS/W*, 173.5 *GOPS/W*, and 286.8 *GOPS/W* when the scale factors for SR are 2, 3, and 4, respectively. Furthermore, we demonstrate that our system can restore HR images with a higher peak signal-to-noise-ratio (PSNR) than conventional SR systems.

Index Terms—Deconvolutional neural networks (DCNNs), convolutional neural networks (CNNs), super-resolution, system architecture.

I. INTRODUCTION

RECENTLY, object detection [1]–[3], recognition [4]–[6], and natural language processing [7] have attracted considerable attention because of the emergence of convolutional neural networks (CNNs). As a result, extensive studies on CNN accelerators have been conducted in order to implement CNN algorithms in real-time systems. In particular, in hardware implementation, FPGA-based CNN accelerators are more energy-efficient than those based on GPUs and can perform

This paragraph of the first footnote will contain the date on which you submitted your paper for review. It will also contain support information, including sponsor and financial support acknowledgment. For example, “This work was supported in part by the U.S. Department of Commerce under Grant BS123456.”

The next few paragraphs should contain the authors’ current affiliations, including current address and e-mail. For example, F. A. Author is with the

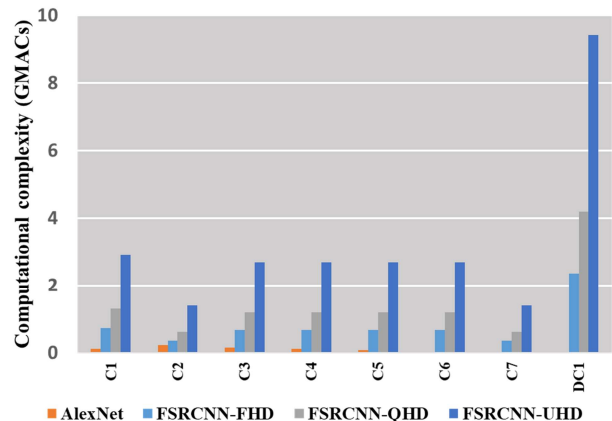


Fig. 1. Comparison of the computational complexity between AlexNet composed of five convolutional layers and FSRCNN composed of seven convolutional layers and one deconvolutional layer, where the convolutional layers are from C1 to C7, and the deconvolutional layer is DC1.

more massive parallel processing than those based on CPUs [8]. In addition, as compared to ASICs FPGAs are sufficiently flexible enough to handle CNNs’ rapid evolution [9], [10].

Most CNN accelerator-related studies [8]–[23] were focused on object detection and recognition applications. In recent years, research studies on image super-resolution (SR) using CNNs have been attracting considerable attention, because the methods proposed can reconstruct images with a higher peak signal-to-noise ratio (PSNR) than conventional methods [24]–[26]. However, since most CNN accelerators are optimized by using object detection and recognition algorithms, the following problems can occur when SR algorithms are implemented in hardware.

First, SR needs a considerably higher resolution image input than object detection and recognition algorithms to generate full-high-definition (FHD), quad-high-definition (QHD), and ultra-high-definition (UHD) videos for mobile applications or TV/broadcasting services. Fig. 1 shows a comparison of the computational complexity of AlexNet [4] and FSRCNN [26], a well-known deep neural networks (DNNs) based SR algorithm. Most object classifiers operate on input images having a pixel resolution of less than 256×256 [4]–[6]. Since the compu-

National Institute of Standards and Technology, Boulder, CO 80305 USA (e-mail: author@boulder.nist.gov).

S. B. Author, Jr., was with Rice University, Houston, TX 77005 USA. He is now with the Department of Physics, Colorado State University, Fort Collins, CO 80523 USA (e-mail: author@lamar.colostate.edu).

T. C. Author is with the Electrical Engineering Department, University of Colorado, Boulder, CO 80309 USA, on leave from the National Research Institute for Metals, Tsukuba, Japan (e-mail: author@nrim.go.jp).

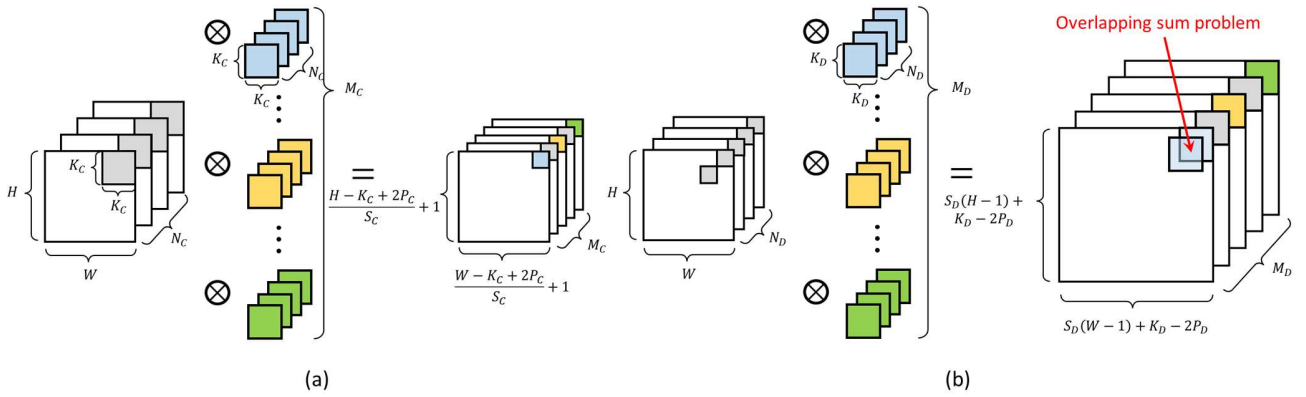


Fig. 2. Comparison of computation schemes for (a) convolutional layer and (b) deconvolutional layer.

tational complexity of CNNs depends on the resolution of the output image, the complexity of FSRCNN requires 38.82 times more giga multiplications-accumulations (GMACs) than AlexNet when generating UHD images.

Second, FSRCNN uses deconvolutional neural networks (DCNNs) [24] at the end of entire network to reconstruct high-resolution (HR) from low-resolution (LR) images. The deconvolutional layer of FSRCNN has a higher computational complexity because it has a maximum of 6.75 times more GMACs than convolutional layers as shown in Fig. 1. Moreover, DCNNs generate up-scaled output blocks in terms of the kernel size as opposed to CNNs, and accumulate pixel values within the output blocks generated from the neighboring pixels. As a result, when DCNNs are implemented in hardware, additional operations are required as compared with CNNs to load the previously obtained output pixels in the memory, update the values of the pixels, and finally store them in the memory. This problem is called the overlapping sum problem [28], [29]. The conventional DCNN accelerator [28] attempts to solve the overlapping sum problem by using formulas to locate the input pixels needed to generate the output pixel through a reverse looping method. Then, a deconvolutional layer processor (DCLP) was designed that performs parallel operations based on the size of tile parameters by applying the loop optimization techniques [10] to deconvolution loops. However, the reverse looping method, which requires additional loads before each processing element (PE), places too heavy a burden on hardware having limited resources. Additionally, the conventional DCNN accelerator does not optimize the high computational complexity of the deconvolutional layer that generates HR images.

In general, using on-chip memory, it is difficult to store all the data required for CNN algorithms, except binarized feature maps [20], because of the large size of the 3D feature maps generated each time the convolutional layer is processed. Therefore, most FPGA-based CNN accelerators use an off-chip memory and perform off-chip data transfer and computation simultaneously through ping-pong operations. As a result, the multiply-accumulate (MAC) operation can be performed continuously through a convolutional layer processor (CLP) using loop optimization techniques [10]. Even if ping-pong operations are applied through double buffers, a CLP cannot

perform the subsequent operation until a large amount of output feature maps are stored in the off-chip memory. In this case, the performance of the accelerators is degraded [18], [19]. In previous papers, CNN fusion architectures were proposed for reducing the large amounts of off-chip data transfers [18], [19]. Fusion architectures are designed with various CLPs for processing multiple convolutional layers within the CNN. Therefore, the data generated after each CLP is operated are transferred to the next layer processor using the on-chip memory. Furthermore, the off-chip data transfer occurs only in the first and last layer of the fused layers. However, these methods still require communication with off-chip memory, which is not energy-efficient.

In this paper, we propose a novel SR-based DNN accelerator for real-time HR image generation with efficient dataflow. The main contributions of this paper are as follows.

- We propose a novel DCNN accelerator that can be massively parallelized by transforming the deconvolutional layer into the convolutional layer (the TDC method). We identified a load imbalance problem during the convolution process executed by the TDC method in our previous work [29]. To overcome this problem, we propose a new load balance-aware TDC method that increases the computation efficiency of the sparse matrix multiplication.
- We propose a dataflow for hardware acceleration to store the intermediate data between the layers using the on-chip memory and to improve the energy efficiency.
- We propose a two-stage quantization algorithm that reduces the size of the CNN for implementing the proposed accelerator in the target FPGA, the hardware resources of which are limited.
- We present an energy-efficient DNN-based SR system. Our system achieves an energy efficiency of 92.7 GOP/W , 173.5 GOP/W , and 286.8 GOP/W when the scale factors for SR are 2, 3, and 4, respectively.

The rest of this paper is organized as follow. Section II gives an overview of the CNN and DCNN algorithms. In Section III, we provide a review of previously proposed architectures. Section IV describes the proposed methodology for the DCNN accelerator. Section V presents the energy-efficient architecture for SR systems and explains the details of the hardware imple-

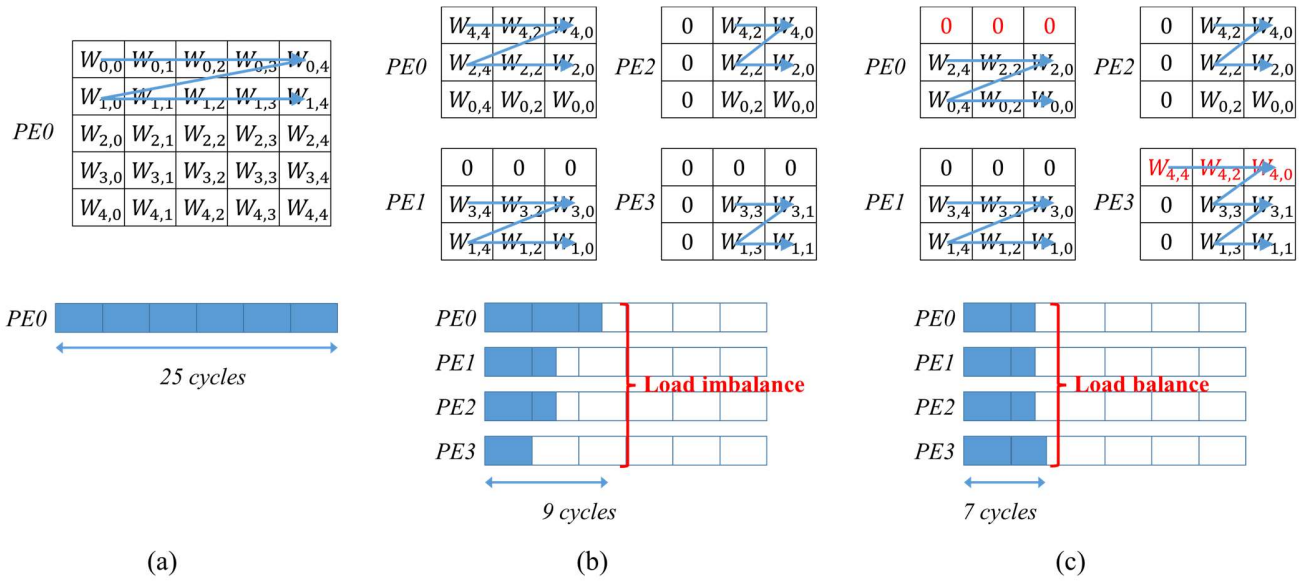


Fig. 3. Advantages of parallelism when TDC and load balance methods are applied. (a) Conventional deconvolutional neural networks (DCNN) accelerator [28]. (b) TDC-based DCNN accelerator [29]. (c) Proposed load balance-aware TDC-based DCNN accelerator.

mentation. Section VI shows a comparison of the experimental results with those of state-of-the-art methods and the results of the hardware implementation. Finally, we conclude this paper in Section VII.

II. BACKGROUND

A. Convolutional Neural Networks

Fig. 2(a) shows the convolutional layer constituting the CNN structure. The convolutional layer receives input feature maps, which are arranged in three dimensions, $H \times W \times N_C$, where H , W , and N_C are the height, width, and the number of input feature maps, respectively. Then, the convolutional layer generates the output feature maps, which are the results of the neurons from the input feature maps obtained using learned weights applied according to procedures inspired by human cognitive science [30]. The process of generating output feature maps is as follows. First, input blocks moving by a defined stride in the input feature maps perform convolution with weights. The kernel size is $K_C \times K_C$, the number of the kernels is $M_C \times N_C$, and the stride is S_C . To generate M_C output feature maps, all the N_C outputs generated by the same type of convolution filter are added together with the biases. Finally, the activation function [31], which abstractly expresses the rate of action potential firing in the cell, transforms the outputs of the three-dimensional convolution. In the FSRCNN, PReLU [32] is used as an activation function. The height and width of the output feature maps generated through the convolutional layer are respectively $\frac{H-K_C+2 \times P_C}{S_C} + 1$ and $\frac{W-K_C+2 \times P_C}{S_C} + 1$, where P_C is the amount of zero padding in the convolutional layer.

B. Deconvolutional Neural Networks

Fig. 2(b) shows the deconvolutional layer that comprises the DCNN. The deconvolutional layer moves the sliding window at stride intervals in the output feature maps rather than in the input feature maps, in contrast to the convolutional layer. In

addition, since deconvolution is performed, the size of the output is the same as the kernel size $K_D \times K_D$. Therefore, as shown in Fig. 2(b), the overlapping sum problem occurs in which the output blocks are overlapped with the neighboring output blocks. Typical accelerators perform tile or line based operations. If the output blocks are created through deconvolution, areas horizontally overlapped with neighboring blocks can easily update the outputs using registers, but vertically overlapping areas must wait until new lines are created. Consequently, it is difficult to store large amounts of intermediate data in on-chip memory to update the previously generated outputs. Until the final outputs are no longer overlapping with neighboring blocks, the processor must read the output that is already stored in memory, and then update it and store it again. Moreover, this inefficient dataflow interferes with the ping-pong operation, which can overlap the computation of the processor with the data transfer time [10]. The height and width of the output feature maps generated through the deconvolutional layer are $S_D \times (H-1) + K_D - 2 \times P_D$ and $S_D \times (W-1) + K_D - 2 \times P_D$, where S_D and P_D are the stride and amount of zero padding in the deconvolutional layer, respectively.

III. RELATED WORK

A. Intra-Layer Parallelism

CNN algorithms require very large amounts of feature maps and weights, because they need to perform the computation of the convolutional layers continuously. Therefore, typical CNN accelerators include a three-level memory hierarchy: 1) off-chip memory, 2) on-chip memory, and 3) PEs. Because of the limitations of on-chip resources, all the data needed for the computation must first be stored in the off-chip memory. The data are then transferred to the CLP via the on-chip memory. For this purpose, three loop optimization techniques [10] have been proposed to efficiently perform computation and data communication within convolution loops in six levels. The

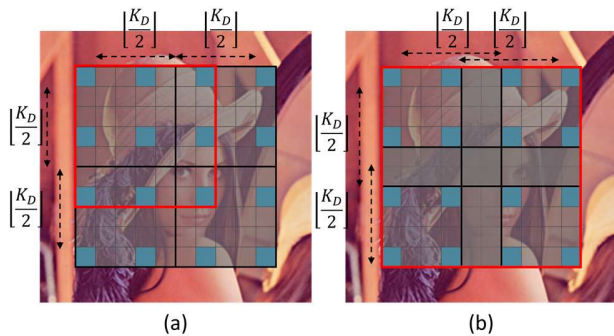


Fig. 4. Examples of overlapping output blocks when fractional values differ. A blue pixel is the center pixel of each output block. The combination of the blue pixels within the red rectangle represents an input block that can produce non-overlapping output. The input block is differently determined when the fractional value of N_o is (a) less than 0.5 and (b) greater than 0.5. In (a) and (b), K_D is 9 and 11, respectively, and S_D is 3 in both.

convolution loops can be executed in parallel with the size of the tile parameters through loop unrolling and tiling techniques. In addition, the computation and off-chip data transfer stages can be performed simultaneously on the same timeline through loop interchange. However, since the pipeline stage length is limited by the off-chip data transfer, the use of the off-chip memory is a major bottleneck in the performance of the accelerators. Data communication through the off-chip memory is one of the major causes of the system's high power consumption and performance degradation. Eyeriss [23] uses an image compression technique to reduce the amount of off-chip data transfer. However, there is a limit to the extent to which data movement can be reduced using lossless compression. In addition, on-chip memory has insufficient capacity to store compressed HR feature maps.

For the conventional DCNN accelerator [28], a reverse looping method was proposed to solve the overlapping sum problem for intra-layer parallelism within deconvolution loops. Then, loop optimization techniques were applied to parallelize the deconvolutional layer, but they did not take into account that the output pixels in the same output feature maps can be generated from the same input blocks. If the source for the new parallelization is applied, the speed of generating HR output feature maps can be improved.

B. Inter-Layer Parallelism

The dimension of the convolutional layers is determined by the convolution filter and is usually different for each layer. Therefore, a design in which a single processor is used can cause a resource underutilization problem [15], [16]. Shen *et al.* [16] proposed a multi-CLP design methodology to solve this problem. Instead of executing convolutional layers on a single large processor, they divided the single large processor into multiple processors to minimize the resources located in an idle state. Then, smaller specialized processors were run simultaneously on the same timeline.

Fusion architectures have been proposed to reduce the off-chip data transfer by executing multiple convolutional layers simultaneously [18], [19]. Alwani *et al.* [18] proposed a method of storing the last feature maps in the off-chip memory after

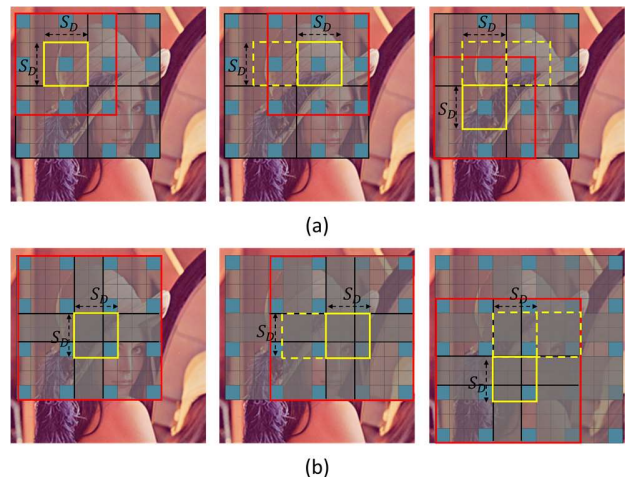


Fig. 5. Example where an $S_D \times S_D$ output block is generated every time a $K_C \times K_C$ input block slides by S_D when the fractional value of N_o is (a) less than 0.5 and (b) greater than 0.5. The blue pixels within the red rectangle are the input pixels and the rectangles enclosed by the yellow solid line and the dotted line represent the output blocks generated from the input blocks of the current and previous positions, respectively.

performing computation in fused convolutional layers. Specifically, the resolution of the feature maps is decreased when passing through the convolutional layer, and the final feature maps are stored in the off-chip memory. Since the on-chip data transfer between fused layers is managed by using the tile-based buffer approach, a burden exists in that exception handling must be included to meet various boundary conditions. To solve this problem, Xiao *et al.* [19] proposed a method of managing feature maps by using line buffers. Even if there are boundaries that require exception handling, data can be easily reused by using several line buffers. However, as the CNN-based SR algorithm has HR feature maps, line buffers cannot easily be utilized because of the burden on the on-chip memory.

IV. PROPOSED DCNN ACCELERATOR

In this section, we propose a load balance-aware TDC method for implementing a DCNN in hardware efficiently. Our method not only involves less computational complexity than conventional method, but also converts deconvolution filters into convolution filters by using a sparse matrix, which is advantageous for hardware implementation. Fig. 3 shows the performance benefits achieved through the proposed load

TABLE I
NOTATIONS FOR DECONVOLUTIONAL LAYER CONFIGURATION

Notation	Explanation
H_I / W_I	Height/width of input feature maps
H_O / W_O	Height/width of output feature maps
M_D / N_D	Number of output/input feature maps
K_D	Kernel size
K_C	Kernel size obtained by applying TDC method to K_C
S_D / P_D	Stride / number of zero padding
T_m / T_n	Tile size for the number of output/input feature maps
\mathbf{W}_D	Weights of the deconvolutional layer
\mathbf{W}_C	Weights obtained by applying TDC method to \mathbf{W}_D

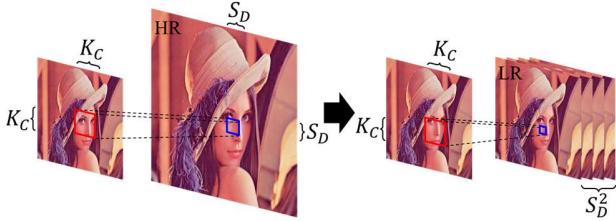


Fig. 6. Visualization when using a new parallelization source in the deconvolutional layer. All the pixels in the $S_D \times S_D$ output block can be created simultaneously.

balance-aware TDC method as compared to other methods. In this case, we used four PEs. Table I shows the notations for the parameters used in the deconvolutional layer.

A. TDC Method

As shown in Fig. 2(b), the pixels in the input feature maps generate an output block of $K_D \times K_D \times M_D$ through the deconvolutional layer. However, there is a problem of overlapping with the output matrix generated from neighboring input pixels. We need to add all the overlapping areas every time the input pixels perform 3D deconvolution. To avoid this overlapping sum problem, we need to determine the number of all the input pixels needed to generate the output in the input space.

Each output block can overlap with adjacent output blocks within a range of $\lfloor \frac{K_D}{2} \rfloor$, as shown in Fig. 4. Because the value of S_D is always greater than 1 for up-scaling, the center pixels between output blocks can never overlap. The total number of cases (N_o) overlapping with neighboring output blocks in $\lfloor \frac{K_D}{2} \rfloor$ can be obtained as

$$N_o = \left\lfloor \frac{K_D}{2} \right\rfloor \times \frac{1}{S_D}. \quad (1)$$

The fractional value of N_o determines how the current output block overlaps with the most distant output block that can be overlapped among adjacent output blocks. Fig. 4 shows a comparison of cases where the integer values are the same but the fractional values differ. As shown in Fig. 4(a), when the fractional value is less than 0.5, it does not overlap within $\lfloor \frac{K_D}{2} \rfloor$ with the most distant output blocks that can be overlapped. Conversely, if the fractional value is greater than 0.5, it overlaps with the most distant output blocks, as shown in Fig. 4(b). Considering both possible cases, the size of the input block, $K_C \times K_C$ that can produce non-overlapping output with the adjacent output block can be determined as

$$K_C = \begin{cases} 2 \times \lfloor N_o \rfloor + 1, & \text{if } N_o - \lfloor N_o \rfloor < 0.5 \\ 2 \times \lceil N_o \rceil, & \text{if } N_o - \lfloor N_o \rfloor \geq 0.5 \end{cases}. \quad (2)$$

Using the property that outputs are generated at the S_D interval in the deconvolutional layer, the $K_C \times K_C$ input block generates the $S_D \times S_D$ output block through the $K_D \times K_D$ deconvolution filters. Fig. 5 shows an example of how $K_C \times K_C$ input blocks slide according to S_D , and thus all the pixels in the $S_D \times S_D$ output block are created. According to the fractional value of N_o , the sliding window, which is shown by the red rectangle, moves sequentially according to S_D and generates the yellow rectangle, which represents an $S_D \times S_D$ output block.

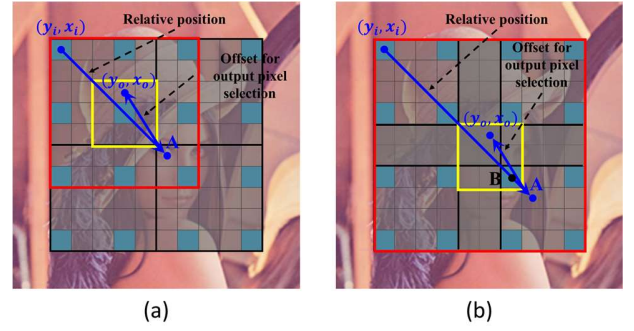


Fig. 7. An example of the inverse coefficient mapping. The method for calculating the relative position between the input pixel and the output block for inverse coefficient mapping depends on (a) when the fractional value of N_o is less than 0.5 and (b) greater than 0.5. The yellow rectangle represents the output block.

The computation process of producing each output pixel consists of MACs between input pixels and weight coefficients. Thereby, each output pixel can be generated from the convolution between the $K_C \times K_C$ input block and the $K_C \times K_C$ convolution filters equal to the size of the input block simultaneously. As shown in Fig. 6, we apply the source of the new parallelization in the hardware implementation for deconvolution. Through the TDC method, the pixels in the $S_D \times S_D$ output block can all be generated simultaneously on the same timeline. Specifically, we convert the spatial domain in the HR output feature map to generate each pixel in the $S_D \times S_D$ output block separately into different channels. Likewise, we apply the TDC method for all output feature maps. Therefore, our TDC method can solve the overlapping sum problem.

B. Inverse Coefficient Mapping

We now describe the acquisition of the weights of the newly created convolutional layer through the TDC method. We declare (x_i, y_i) , (x_d, y_d) , and (x_o, y_o) as the indices of an input pixel mapped to an output feature map, a weight coefficient of a deconvolutional layer, and an output pixel, respectively. The range of each pixel is defined as

$$\begin{aligned} 0 \leq x_i < K_C, \quad 0 \leq y_i < K_C \\ 0 \leq x_d < K_D, \quad 0 \leq y_d < K_D. \\ 0 \leq x_o < S_D, \quad 0 \leq y_o < S_D \end{aligned} \quad (3)$$

For mapping the weights of the deconvolutional layer to those of the convolutional layer, we propose an inverse coefficient mapping process to find (x_d, y_d) corresponding to (x_i, y_i) . Fig. 7 shows an example of the inverse coefficient mapping. The inverse coefficient mapping process is as follows.

We need to find the weight coefficient that should be convolved with the input pixel at (x_i, y_i) to generate the output pixel in the $S_D \times S_D$ output block. Since (x_i, y_i) is the centered index of the output block generated after deconvolution, the index of the coefficient to be multiplied by (x_i, y_i) can be obtained by two factors, the relative position between (x_i, y_i) and the output block, and the offset to select (x_o, y_o) , as illustrated in Fig. 7.

First, we can obtain the relative position between (x_i, y_i) and the output block as $(K_D - S_D \times x_i, K_D - S_D \times y_i)$. However, since output blocks are created in two types according to the fractional value of N_o , their relative position also depends on

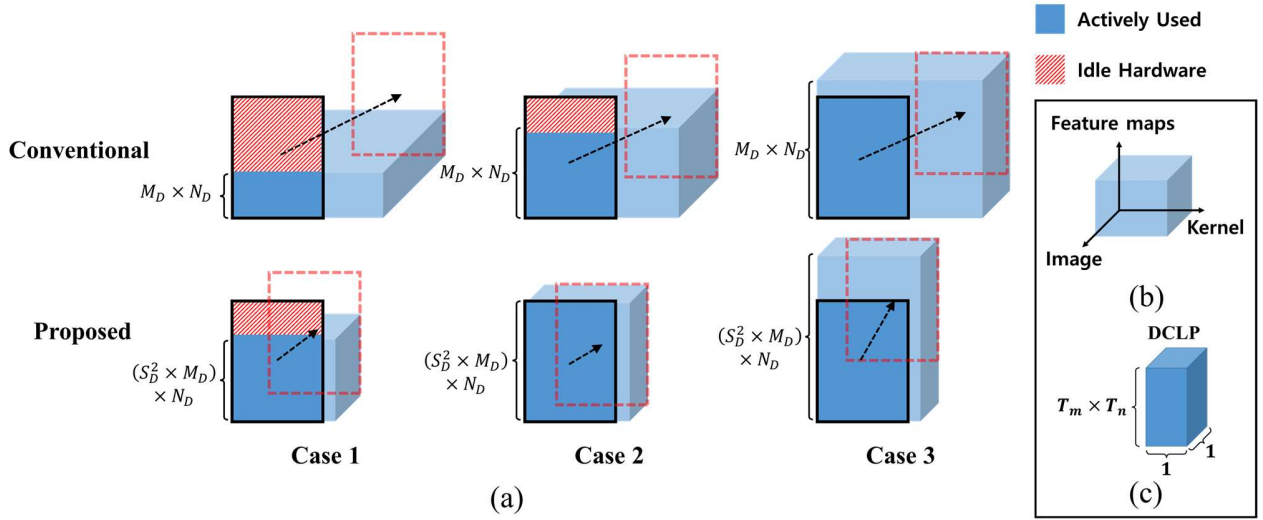


Fig. 8. Operation of deconvolutional layer processor (DCLP) on a one-layer deconvolutional neural network. (a) The difference between the proposed method and the conventional method depending on the range of M_D . (b) Three-dimensional visualization of computational complexity for deconvolution loops. (c) The DCLP that parallelizes the output feature maps and the input feature maps with tiling parameters T_m and T_n .

this value. Fig. 7(a) shows that, if the fractional value of N_O is less than 0.5, the relative position between (x_i, y_i) and the output block is always point A. Conversely, Fig. 7(b) shows that, if the fractional value of N_O is greater than 0.5, the relative position is always point B, because the indices of the output block are decremented by 1. To adjust both situations to the same position, we add 1 if the fractional value of N_O is greater than 0.5. Accordingly, the relative position between the input pixel and the output block corresponding to the coefficient (x_r, y_r) can be obtained as

$$\begin{aligned} x_r &= \begin{cases} K_D - (S_D \times x_i), & \text{if } N_O - \lfloor N_O \rfloor < 0.5 \\ K_D + 1 - (S_D \times x_i), & \text{if } N_O - \lfloor N_O \rfloor \geq 0.5 \end{cases} \\ y_r &= \begin{cases} K_D - (S_D \times y_i), & \text{if } N_O - \lfloor N_O \rfloor < 0.5 \\ K_D + 1 - (S_D \times y_i), & \text{if } N_O - \lfloor N_O \rfloor \geq 0.5 \end{cases} \end{aligned} \quad (4)$$

Next, we subtract the offset to select the coefficient for one of the output pixels. We can obtain the indices of the weight coefficient corresponding to the input pixel as

$$\begin{aligned} x_d &= x_r - (S_D - (x_o \bmod S_D)) \\ y_d &= y_r - (S_D - (y_o \bmod S_D)) \end{aligned} \quad (5)$$

Finally, \mathbf{W}_D , which represents the weights of the deconvolutional layer, is mapped to the weights of the newly created convolutional layer, \mathbf{W}_C :

$$\begin{aligned} \mathbf{W}_C[S_D^2 \times m + S_D \times y_o + x_o][n][y_i][x_i] &= \\ \mathbf{W}_D[m][n][y_d][x_d] \end{aligned}, \quad (6)$$

where m and n are iterators for loops of the output and input feature maps, respectively.

C. Zero-Aware Processing Element

Our TDC method maps the $K_D \times K_D$ weights to a matrix of $K_C \times K_C \times S_D^2$ size in each input and output feature map. Because \mathbf{W}_C and \mathbf{W}_D are not the same size, there are zero-valued elements. The number of zero-valued elements, num_{zero} , in the transformed convolution kernels is derived as

$$num_{zero} = (K_C^2 \times S_D^2 - K_D^2) \times M_D \times N_D. \quad (7)$$

Table II shows the ratio of zero weights in the convolutional layer generated by the TDC method. The ratio varies according to K_D and S_D . Moreover, it can be seen that K_C obtained from the TDC method is always smaller than K_D .

The TDC method can generate output pixels in parallel by reducing the kernel size of the weights. However, the load imbalance problem occurs because of the zero weights in most cases, as shown in Table II. This is because the distribution of \mathbf{W}_C is different for each output pixel. Fig. 3(b) shows the performance degradation of each PE caused by the load imbalance problem. To efficiently process sparse matrix multiplication in parallel, we propose the load balance-aware TDC method as shown in Fig. 3(c). Previously, $PE0$ contained nine non-zero weights, whereas $PE3$ contained four non-zero weights. The pipeline stage is determined by $PE0$, which requires the most computational complexity. However, the position of zero weights is always the same for each deconvolutional layer, since the inverse coefficient mapping applies equally to all kernels. Therefore, it is not necessary to find the position of non-zero weights for each operation.

By using the load balance-aware TDC method, we minimize the execution cycles by evenly distributing non-zero weights across the PEs.

D. Performance Enhancement

After applying the load balance-aware TDC method, we parallelized the input and output feature maps using the loop

TABLE II
ZERO WEIGHT RATIO OF CONVOLUTIONAL LAYER CREATED BY THE TDC METHOD

K_D	S_D	K_C	Zero Weights [%]
9	2	5	19
9	3	3	0
9	4	3	43.8
7	2	4	23.4
7	3	3	39.5
7	4	2	23.4
5	2	3	30.6
5	3	2	30.6
5	4	2	60.9

TABLE III
FSRCNN CONFIGURATION AFTER TDC METHOD

Layer	1	2	3	4	5	6	7	8
N_C	1	56	12	12	12	12	12	56
M_C	56	12	12	12	12	12	56	S_D^2
H_C	H_I	H_I	H_I	H_I	H_I	H_I	H_I	H_I
W_C	W_I	W_I	W_I	W_I	W_I	W_I	W_I	W_I
								$S_D=2$ 5
K_C	5	1	3	3	3	3	1	$S_D=3$ 3
								$S_D=4$ 3
S_C	1	1	1	1	1	1	1	1

optimization techniques to make a comparison with the conventional DCNN accelerator in the same environment. The execution cycles of the deconvolutional layer are

$$\begin{aligned} & \text{Execution cycles} \\ &= \left\lceil \frac{S_D^2 \times M_D}{T_m} \right\rceil \times \left\lceil \frac{N_D}{T_n} \right\rceil \times \frac{H_O}{S_D} \times \frac{W_O}{S_D} \times \left\lceil \frac{K_D^2}{S_D^2} \right\rceil. \\ &= \left\lceil \frac{S_D^2 \times M_D}{T_m} \right\rceil \times \left\lceil \frac{N_D}{T_n} \right\rceil \times H_I \times W_I \times \left\lceil \frac{K_D^2}{S_D^2} \right\rceil \end{aligned} \quad (8)$$

There are three different cases of performance enhancement as compared to the conventional DCNN accelerator, depending on the range of M_D , as shown in Fig. 8. Fig. 8(a) shows a visualization of the difference in the performance of the conventional and the proposed method for each case. Both methods were executed on the same DCLP. A visualization of the total computational complexity at the deconvolutional layer is shown in Fig. 8(b). Fig. 8(c) shows the hardware size for the DCLP. In the rectangular parallelepiped, the width and height of the bottom surface represent the size of the tiling parameters for the kernel and image, respectively. Because the DCLP performs parallel processing on the input and output feature maps, both lengths are equal to 1.

Case 1. $M_D \leq \frac{T_m}{S_D^2}$

Although the number of output feature maps is S_D^2 times larger than previously, our proposed method unrolls the entire loops for the output feature maps. In addition, our method improves the resource underutilization problem, where idle hardware exists in the DCLP. Furthermore, our method reduces the convolution cycle and generates LR instead of HR images. As a result, the width and height of the bottom surface become smaller. The performance enhancement is

$$\text{Performance enhancement} = S_D^2 \times \frac{K_D^2}{\left\lceil \frac{K_D^2}{S_D^2} \right\rceil}. \quad (9)$$

Case 2. $\frac{T_m}{S_D^2} < M_D \leq T_m$

Our method completely solves the resource underutilization problem by activating all T_m - M_D hardware resources that are in the idle state. The width and height of the bottom surface are reduced, as in Case 1. The performance enhancement is

$$\text{Performance enhancement} = \frac{S_D^2}{\left\lceil (S_D^2 \times M) / T_m \right\rceil} \times \frac{K_D^2}{\left\lceil K_D^2 / S_D^2 \right\rceil}. \quad (10)$$

Case 3. $M_D \geq T_m$

TABLE IV
NOTATIONS FOR l^{th} CONVOLUTIONAL LAYER CONFIGURATION

Notation	Explanation
H^l / W^l	Height/width of input feature maps
H^{l+1} / W^{l+1}	Height/width of output feature maps
M^l / N^l	Number of output/input feature maps
K^l	Kernel size
S^l / P^l	Stride / number of zero padding
T_y^l / T_x^l	Tile size for height/width of input feature maps
T_m^l / T_n^l	Tile size for number of output/input feature maps
T_k^l	Tile size for kernel size

Our method cannot process in parallel more output feature maps than the existing DCNN accelerator. However, the execution speed is faster, because the computational complexity of the PE is reduced, and the efficiency of the matrix multiplication is improved through the load balance. The performance enhancement is

$$\text{Performance enhancement} = \frac{S_D^2 \times \left\lceil M / T_m \right\rceil}{\left\lceil (S_D^2 \times M) / T_m \right\rceil} \times \frac{K_D^2}{\left\lceil K_D^2 / S_D^2 \right\rceil}. \quad (11)$$

We will show the results of quantitative evaluation in popular models including DCNN in Section VI.

V. PROPOSED DNN-BASED SUPER-RESOLUTION SYSTEM

In this section, we propose novel methodologies to achieve an energy-efficient SR architecture for implementing the state-of-the-art DNN-based SR algorithm, FSRCNN. Table III shows the new FSRCNN configuration after the load balance-aware TDC method was applied.

A. Dataflow Optimization with On-Chip Memory

In our system, which does not use off-chip memory, the FPGA receives the pixel through the display driver in the horizontal direction of the frame. When all the pixels in the frame have been transferred, the data for the next frame are sent to the FPGA. If all the convolutional layers are executed by a single CLP, the pixel data coming into the FPGA must be stored in the on-chip memory until the last layer is completely processed. Consequently, several frame buffers may be required, depending on the execution time of the CLP. In order to solve this problem, we process the input data coming into the FPGA by designing all the convolutional layers such that they run concurrently through multiple CLPs, as in fusion architectures [18], [19]. In this case, the multiple CLPs must be designed such that they can handle on-chip dataflow efficiently. Thus, the loop tiling parameters of each CLP must be determined. To find the loop tiling parameters, we compare the computation speed of each CLP with the speed of the pixel data coming into it.

Table IV shows the notations for the l^{th} convolutional layer needed to optimize the dataflow, where the range of l is $1 \leq l \leq L$. L is the index of the last layer, the deconvolutional layer. We treat the deconvolutional layer as a convolutional layer through the load balance-aware TDC method. The computation to transmission (CT) ratio is defined as the ratio of the cycles required to perform the l^{th} CLP to the cycles required to transmit

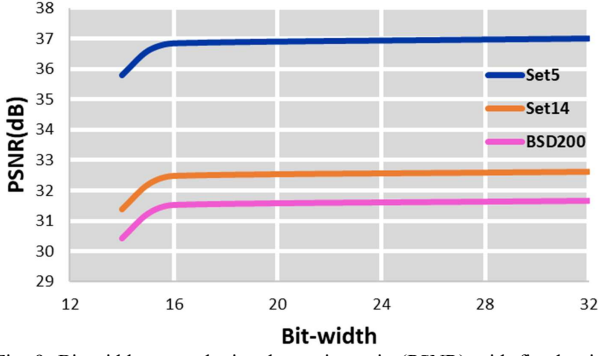


Fig. 9. Bit-width vs. peak signal-to-noise ratio (PSNR) with fixed-point quantization technique when the up-scaling factor is set to 2.

the pixel data from the display driver or input buffers to the l^{th} CLP. When the tile size combination of the l^{th} CLP is given as $T_y^l, T_x^l, T_m^l, T_n^l$, and T_k^l , illustrated in Table IV, the l^{th} CT , which is CT^l , is calculated as

$$\begin{aligned}
 CT^l \text{ ratio} &= \frac{\text{total number of execution cycles}}{\text{total number of transmission cycles}} \\
 &= \frac{H^l \times W^l \times \left\lceil \frac{M^l}{T_m^l} \right\rceil \times \left\lceil \frac{N^l}{T_n^l} \right\rceil \times \left\lceil \frac{K^l}{T_k^l} \right\rceil \times \left\lceil \frac{K^l}{T_k^l} \right\rceil}{H^l \times W^l \times \left\lceil \frac{N^l}{T_n^l} \right\rceil} \quad (12) \\
 &= \left\lceil \frac{M^l}{T_m^l} \right\rceil \times \left\lceil \frac{K^l}{T_k^l} \right\rceil \times \left\lceil \frac{K^l}{T_k^l} \right\rceil
 \end{aligned}$$

We do not consider T_y^l and T_x^l when calculating CT^l , because the input of each CLP is sequentially transmitted in pixel data instead of tile-sized pixel blocks. If the value of CT^l is greater than 1, the transmission speed of the pixel data in the l^{th} layer is faster than that of the CLP, and hence, the data transferred during the computation must be stored in the frame buffer. For example, if an output image with UHD is generated using an SR algorithm with a scale factor of 2, approximately 8.1 MB buffer memory is required to store an input image with a 1920×1080 resolution in the 32-bit floating-point data type. Furthermore, considering the size of the input feature maps, it can exceed the allowable on-chip memory of a typical FPGA. For this reason, we set the CT of all layers to a value of 1 in order not to use the frame buffer. Hence, T_m^l and T_k^l become M^l and K^l , respectively. In addition, the tiling factors of the input feature maps of the next layer, T_n^{l+1} and T_m^l , should be the same so that the feature maps can be transmitted without buffering to the next layer. Since N^{l+1} is equal to M^l , T_n^l also becomes equal to N^l . As a result, all the CLPs can fully process the three convolution loops in parallel.

A memory management technique is required to efficiently store the feature maps generated by multiple CLPs. Since the pixel data from the display driver are transmitted line by line, we use a line buffer that can reuse the data without being restricted by boundary conditions [19]. The line buffer is designed as a block RAM (BRAM), that is, a simple dual-port mode [33] in which one read and one write are allowed concurrently in order to fulfill both the input and output buffer of each CLP. Although there may be separate input buffers and output buffers for each CLP, we share input and output buffers

Algorithm 1: Two-stage quantization algorithm

```

Input:  $\mathbf{M} = \{M^1, \dots, M^L\}$ ,  $\mathbf{K} = \{K^1, \dots, K^L\}$ 
Output:  $\text{best\_M}_q = \{M_q^1, \dots, M_q^L\}$ ,  $\text{best\_K}_q = \{K_q^1, \dots, K_q^L\}$ 
1   $\mathbf{G}_M[0:2], \mathbf{G}_K[0:2] = \text{Group}(\mathbf{M}, \mathbf{K})$ 
2   $R = \text{receptive\_fields}(K^1, \dots, K^L)$ ;
3   $R_0 = R$ ;  $\mathbf{G}_K^q[0:2] = \mathbf{G}_K[0:2]$ ;  $\mathbf{G}_M^q[0:2] = \mathbf{G}_M[0:2]$ ;
4  for ( $i = 0$ ;  $R - R_i < \text{threshold}_1$ ;  $i = i + 1$ ) do // First stage. kernel quantization
5       $\mathbf{G}_K^q[0:2] = \text{kernel\_quantization}(\mathbf{G}_K[0:2], i)$ ;
6       $R_{i+1} = \text{receptive\_fields}(\mathbf{G}_K^q[0:2])$ ;
7      for ( $j = 0$ ;  $j < \text{threshold}_2$ ;  $j = j + 1$ ) do // Second stage. feature quantization
8           $\mathbf{G}_M^q[1] = \mathbf{G}_M^q[1] - j$ ;
9           $\mathbf{G}_M^q[0] = \text{feature\_quantization}(\mathbf{G}_M[0], \text{numDSP}(\mathbf{G}_M[0:2], \mathbf{G}_K[0:2]))$ ;
10         if ( $\text{numDSP}(\mathbf{G}_M[0:2], \mathbf{G}_K[0:2]) > \text{total\_DSPs}$ )
11             continue;
12          $\text{model} = \text{caffe\_training}(\mathbf{G}_M^q[0:2], \mathbf{G}_K^q[0:2])$ ;
13          $\text{best\_model} = \text{compare}(\text{model}, \text{best\_model})$ ;
14          $R_{i+1} = \text{receptive\_fields}(\mathbf{G}_K^q[0:2])$ ;
15   $\text{best\_M}_q, \text{best\_K}_q = \text{extract}(\text{best\_model})$ ;
  
```

between CLPs via the simple dual port mode. The capacity needed to implement the line buffer should be same as the size of the 3D data generated from the CLP. In addition, the number of line buffers must be equal to the width of the kernel size for the convolution. Therefore, the size of the input and output buffers for the l^{th} CLP, which are M_{in}^l and M_{out}^l respectively, can be calculated as

$$\begin{aligned}
 M_{in}^l &= K^l \times W^l \times N^l \times \text{datawidth}, \\
 M_{out}^l &= \begin{cases} K^{l+1} \times W^{l+1} \times N^{l+1} \times \text{datawidth}, & \text{if } l < L \\ S^l \times (S^l \times W^l) \times \text{datawidth}, & \text{otherwise} \end{cases} \quad (13)
 \end{aligned}$$

In the case of the deconvolutional layer, the size of the output buffer is calculated using S^l instead of K^{l+1} , because an $S^l \times S^l$ output block is generated. Moreover, the width of the image is scaled up S^l times.

Consequently, we unroll all three convolution loops to avoid frame buffering, and therefore, the output of the neurons becomes the input of the next neurons without the accumulation of other neurons. In this manner, the output feature maps generated by the convolutional layer in front of the 1×1 convolutional layer can be directly sent to the CLP of the 1×1 convolutional layer without being stored in the output buffer. FSRCNN has two 1×1 convolutional layers. One is called the shrinking layer and the second is called the expanding layer. The shrinking layer compresses the largest input feature maps into a reduced size. When the CLPs of the shrinking layer and the preceding layer are combined, there is an advantage that there is no need to store a large amount of intermediate data in the buffer. Conversely, the expanding layer restores the reduced input feature maps to the original size. Even when it is combined with the forward layer, there is little benefit in reducing the buffer capacity because the number of input feature maps in the expanding layer is reduced by means of the shrinking layer. If T_y of the expanding layer is set to the width of the kernel size of the backward layer, it may not buffer a large number of output feature maps generated in the expanding layer. However, since there is a tradeoff between the buffer and CLP

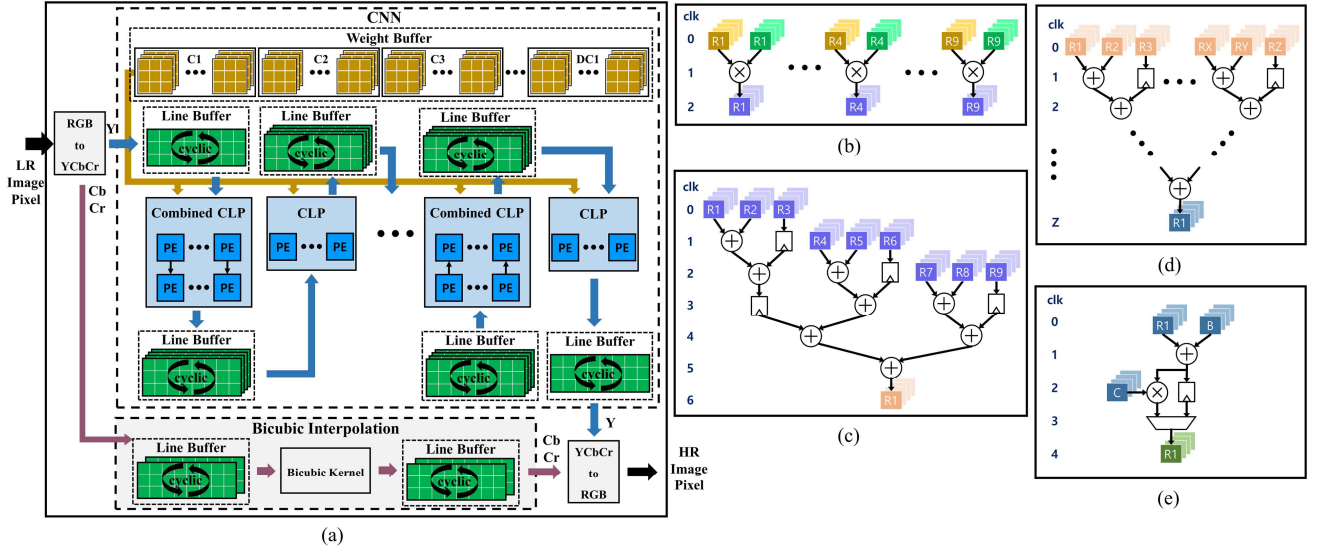


Fig. 10. (a) Overview of the proposed architecture. The processing element consists of (b) multiply engine for kernel-sized convolution, (c) add engine for kernel-sized convolution, (d) add engine for adding all of the input feature maps to generate each output feature map, and (e) activation engine for generating output of neuron.

size, we combine all 1×1 layers with the forward layer.

According to the guideline [33], a 7 series FPGA BRAM-18kb unit can store 512 32-bit words. With 32-bit words, the line buffers used in our system could be built with $\sum_{l=1}^L \left[\frac{M_l^l}{512} \right] + \left[\frac{M_{out}^l}{512} \right]$ BRAMs. Hence, the number of BRAMs required to generate a UHD image was 1609, which is greater than that in a typical FPGA. Thus, it was necessary to reduce the usage of BRAMs for the utilization of embedded systems. We describe the reduction of BRAM usage through the CNN model quantization method in Section C.

B. Quantized FSRCNN (QFSRCNN)

Fixed-point implementation mitigates the complexity of hardware design and potentially enables the use of embedded hardware [34]. In particular, our CLPs are 3D CLPs that process three convolution loops in parallel, and therefore, the implementation of hardware with a fixed-point increases resource utilization efficiency. Fig. 9 shows the PSNR ratio according to the bit-width of the data in the representative datasets, Set5, Set14, and BSD200. In Fig. 9, it can be seen that the PSNR decreases when the bit-width is smaller than 16-bit, while the performance is maintained when the bit-width is larger than 16-bit. To optimize the utilization of the FPGA resources more compactly, pixels, weights and partial sums are expressed as 16-bit fixed-points reduced from the 32-bit single-precision floating-points using the bit-width quantization method [35]. For all line buffers, the number of BRAMs is halved for the 16-bit fixed-point precision. This is because 16-bit word pairs are packed into 32-bit wide BRAMs.

The number of DSPs required for the multiplier and adder of the Xilinx Kintex-7 FPGA, the hardware implemented for the SR system, is one each with the precision of a 16-bit fixed-point. If the multiplier and adder are implemented as logic elements in the FPGA, the required resources are 280 LUT6s and 16

LUTs+16 FFs, respectively. When completely unrolling several convolution loops, we cannot use both multipliers and adders as DSPs because of the limited number of DSPs. Therefore, we designed an adder with LUTs and FFs, which require a smaller number of logic elements than a multiplier, and a multiplier with a DSP. The total number of DSPs required in the design of the multiple CLPs was

$$num_{DSP} = \sum_{l=1}^L M^l \times N^l \times K^l \times K^l - num_{zero}, \quad (14)$$

where num_{zero} , defined in Eq.(7), is the number of zero-valued weights in the transformed convolution filters.

The number of DSPs required for FSRCNN is 8180, which is greater than the total number of DSPs in high-end FPGAs. For this reason, we propose a two-stage quantization algorithm to reduce the model size of the FSRCNN. Algorithm 1 represents the pseudo code for the two-stage quantization algorithm. It is used to find the best CNN model that can be implemented in the target FPGA.

We define the fundamental problem for designing the SR system to maximize the performance and implementing it in the target FPGA. The problem can be formulated as

$$\text{maximize } PSNR_i, \quad \text{s. t. } num_{DSP_i} \leq total \text{ DSPs.} \quad (15)$$

where $PSNR_i$ and num_{DSP_i} are the PSNR value and the number of DSPs needed for the i^{th} combination of possible configurations, respectively. We do not include memory constraints, because the fixed-point quantization solves this problem.

We needed to perform an exhaustive search for all configurations to find the optimal quantized model, because the objective function $PSNR_i$ is obtained through training. Several experiments were conducted to determine the parameters of each layer in FSRCNN, and a threshold at which the PSNR did not increase, although the size of the parameters was increased,

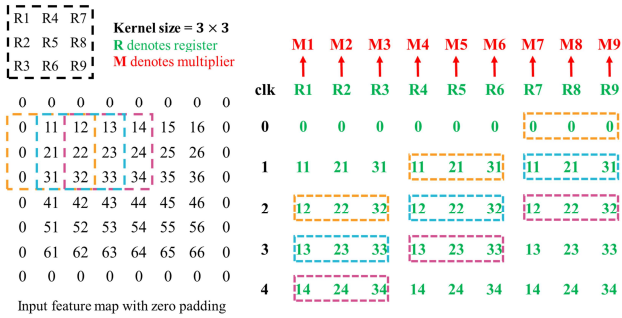


Fig. 11. Dataflow example of incoming input pixels through each line buffer for the convolution operation. The registers are from R1 to R9 and the multipliers are from M1 to M9.

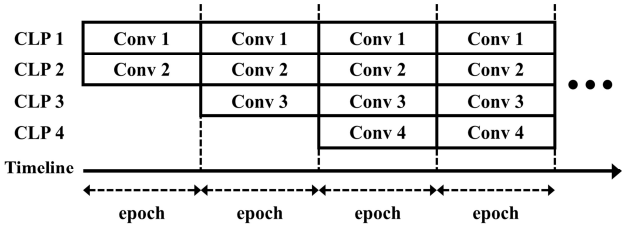


Fig. 12. Example schedule for our system.

was found. Thereby, when reducing the CNN model, we define a new objective function that replaces the PSNR, assuming that the number of parameters in the CNN model is closely related to the performance. The number of parameters in the CNN model is determined by the kernel size and the number of feature maps. We divide into two stages the procedure to determine respectively the kernel size and the number of feature maps for each layer.

In the first stage, we calculate the size of the receptive field to determine how many surrounding pixels are used. The receptive field R has the size of the input block required to generate the pixel for the output feature maps of the last layer. Thus, we repeatedly reduce R in the first stage of our algorithm. R can be calculated as

$$R = K^1 + 2 \times \sum_{l=2}^L \left\lfloor \frac{K^l}{2} \right\rfloor. \quad (16)$$

By Eq. (16), the size of the receptive field in the FSRCNN is 17×17 . We need to find the best receptive field among the various cases in the first stage. However, as there are many configurations, we limit the size of the receptive field using $threshold_1$. In Algorithm 1, we repeatedly quantize the kernel size until $R-R_i$ is greater than $threshold_1$.

In the second stage, we determine the number of output feature maps for each layer, because the number of output feature maps in the current layer is equal to the number of input feature maps in the next layer. We simply set the objective function for reducing the output feature maps O as $\prod_{l=1}^L M^l$, however, the problem arises that the number of the variable M^l is the same as the total number of layers L in the CNN. We mitigate this problem by grouping layers with similar characteristics. FSRCNN is an hourglass-type CNN, as shown in Table III. Unlike those of the other layers, the output feature maps of the deconvolutional layer are excluded from the

TABLE V
 QUANTIZED FSRCNN CONFIGURATION AFTER LOAD BALANCE-AWARE TDC METHOD AND TWO-STAGE QUANTIZATION ALGORITHM

Layer	1	2	3	4	5	6	7	8
N_C	1	22	4	4	4	4	4	22
M_C	22	4	4	4	4	4	22	S_D^2
H_C	H_l	H_l	H_l	H_l	H_l	H_l	H_l	H_l
W_C	W_l	W_l	W_l	W_l	W_l	W_l	W_l	W_l
K_C	3	1	3	3	3	3	1	$S_D=2$ 3 $S_D=3$ 3 $S_D=4$ 3
S_C	1	1	1	1	1	1	1	1

quantization, because each feature map is merged into an HR image. Thus, except for the deconvolutional layer, there are two groups of layers with the same number of output feature maps. We describe the differential of O for the feature maps as dO/dM^l . We can represent a set of layers with the same dO/dM^l and create vectors containing their configurations. For example, the first and seventh layer have the same dO/dM^l , but are smaller than the other layers. In consequence, these layers belong to the set $\mathbf{G}[0]$ and the layer configurations are stored in $\mathbf{G}_M[0]$ and $\mathbf{G}_K[0]$, respectively, which represent the sets containing the number of output feature maps and the kernel size. The value of dO/dM^l in the deconvolutional layer is larger than that of the other groups and it belongs to $\mathbf{G}[2]$. Nevertheless, they cannot be reduced and excluded from optimization. A set with a higher index value has a larger value of dO/dM^l than a set with lower index value. Therefore, we solve the objective function O separately for each set. In Algorithm 1, the number of output feature maps included in $\mathbf{G}_M^q[1]$ is reduced according to $step$. We then determine the number of output feature maps included in $\mathbf{G}_M^q[1]$ with the remaining DSPs through $\left\lfloor \frac{total\ DSPs - \delta}{\tau} \right\rfloor$, where τ is the quantized kernel size and δ is the number of DSPs for the layers in the other sets. Consequently, in the second stage, we first quantize the output feature maps $\mathbf{G}_M^q[1]$ of the layers belonging to set $\mathbf{G}[1]$ without considering $\mathbf{G}_M^q[0]$. Then, the output feature maps of the layers belonging to $\mathbf{G}[0]$ are quantized. Then, we increment $\mathbf{G}_M^q[0]$ by gradually decrementing the values of $\mathbf{G}_M^q[1]$ until the loop iterator is greater than the $threshold_2$. We repeat this process with the first stage, learn through the Caffe framework [36], and compare the newly learned models with the best model. Table V shows the configuration of the quantized FSRCNN (QFSRCNN) model through the two-stage quantization algorithm. In order to implement the CNN accelerator as an on-chip FPGA, we reduced the total number of parameters by approximately 82%.

C. Hardware Implementation

Fig. 10(a) shows the proposed on-chip memory-based FPGA architecture. The FPGA receives the input of the LR image composed of RGB data and uses the Y channel as input after performing the data conversion from RGB to YCbCr as the first step of the SR system. In general, in DNN-based SR system, the Cb and Cr channels are rarely used for learning [25]. The reason is that these channels contain less important information than

TABLE VI
PERFORMANCE COMPARISON OF DCNN ACCELERATORS

		CLP Configuration			[28]	Ours
Model	Layer	S_D	T_m	T_n	Cycles \times 1000	Cycles \times 1000
DCGAN	1	2	4	128	1,638	458
	2	2	4	128	1,638	458
	3	2	4	128	1,638	458
	4	2	4	128	102	21
	Total				5,017	1,397
FSRCNN	8	2	56	9	21,233	1,376
	8	3	56	9	47,775	589
	8	4	56	9	84,934	786

the Y channel. As a result, we upscale the Cb and Cr channels with bicubic interpolation.

According to ITU-R Recommendation BT.601-5 [37], RGB-to-YCbCr conversion requires floating-point arithmetic. Even if the RGB-to-YCbCr conversion is implemented as a fixed-point operation for the embedded hardware, quantization errors rarely occur [38]. Moreover, fixed-point arithmetic has the advantage of being able to evolve into shift operations, and therefore, we designed the RGB-to-YCbCr conversion with 16-bit fixed-point precision. Likewise, we also implement YCbCr-to-RGB conversion in a hardware-friendly fashion, with shift operations and the adder executed at the end of the system.

Before entering the CLP, the pixel data are stored in the line buffers. After K^l-1 lines are stored, the outputs of the line buffers and incoming data enter the CLP and perform the convolution with the filters from the weight buffer. The CLP of the first layer and the CLP of the 1×1 layers, the shrinking layer, are fused into the combined CLP. In addition, the CLP of the sixth layer and the CLP of the 1×1 layer, the expanding layer, are fused into another combined CLP. Intermediate data that require a large amount of memory in each combined CLP are not stored in the line buffers. Thus, the combined CLP reduces the total amount of line buffers to 81%. We store the weights of all the convolutional layers in read-only memory (ROM); the size of the weights is only 3 KB, which is acceptable for on-chip memory.

Fig. 10(b)–(e) shows the computation engines in the PE constituting the CLP. First, the PE fetches the data stored in the line buffer into the registers and performs multiplication with weights. We perform all the multiplication operations within the kernel at the same time and process these operations $M^l\times N^l$ times in parallel as depicted in Fig. 10(b). Then, we add the outputs of the multiplication through the adder tree, but do not add the outputs of the multipliers in the same timeline, as shown in Fig. 10(c). Because each line buffer exports K^l data per clock cycle to the PEs, the K^l register pairs have the same inputs when multiplying with the kernel. Fig. 11 illustrates the dataflow of the input pixels in the input feature map with zero padding for the convolution operation. At clock cycle 0, all the registers are loaded with zero padded values. Among the registers, R7–R9 store the valid data, because they are the initial values for the convolution operation. Then, in cycle 1, the sliding window in the input feature map moves to the right according to the stride value and the new values are loaded into the registers. The

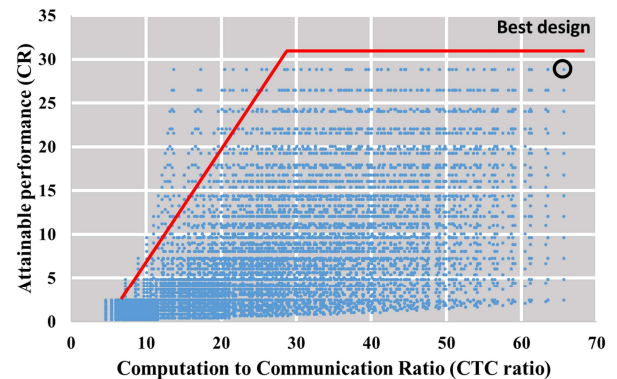


Fig. 13. Example of design space exploration.

initial values for the next convolution are loaded into R7–R9; a yellow box equal to cycle 0 is the register array for the same result. In cycle 3, valid input pixels begin loading into R1–R3 and are the last inputs of the adder tree shown in Fig. 10(c). Thus, the convolution between input pixels and weights is fully pipelined. Fig. 10(d) shows the process of adding the results of each input feature map through the add engine consisting of M^l adder trees. Finally, Fig. 10(e) shows the output of the neurons via the PReLU activation engine. The activation engine generates M^l outputs simultaneously. Fig. 12 shows that the convolutional layers are performed on the pipeline through the proposed architecture. All the layers are executed concurrently on the same timeline. For layers where the width of the kernel size is greater than 1, there is a line delay until K^l lines are filled before the CLPs are fully pipelined.

VI. EXPERIMENTAL RESULTS

In this section, we show the efficacy of the DCNN accelerator based on the load balance aware-TDC method and the proposed on-chip memory-based SR system with FPGA. First, we compare the performance of the proposed DCNN accelerator with that of the state-of-the-art method. Then, we evaluate the performance of the proposed SR system.

A. Evaluation of the Proposed DCNN Accelerator

We validated the DCNN accelerators with the Xilinx Virtex-7 485T FPGA in the same experimental environment as that used in the study in [29]. We implemented the proposed and the conventional architecture using Vivado HLS 2016.4 and used a single-precision floating-point. We evaluated the DCNN models, FSRCNN and DCGAN [39], implemented in the hardware used in previous studies [28], [29]. To compare the performance of the proposed DCNN accelerator in the same experimental environment as the conventional DCNN accelerator, we designed the accelerator using the single CLP method [10]. The conventional DCNN accelerator paralleled the convolution loops for output feature maps and input feature maps with T_m and T_n , respectively, and determined the optimal tiling parameters through the roofline model [40]. Fig. 13 shows possible design space solutions when designing the CLP for the fourth layer of the FSRCNN by means of the roofline model. The computation to communication (CTC) ratio is the ratio of the number of operations performed per external memory

TABLE VII
PERFORMANCE COMPARISON WITH STATE-OF-THE-ART CNN AND DCNN ACCELERATORS (FX: FIXED-POINT, FT: FLOATING-POINT)

	[12]	[21]	[13]	[17]	[21]	[22]	[18]	[19]	[28]	This Work
	AlexNet	AlexNet	VGG16	VGG16	VGG16	VGG16	VGG19	VGG19	DCGAN	QFSRCNN
FPGA	Startix-V GXA7	Startix-V GXA7	Zynq XC7Z045	Arria-10 GX1150	Startix-V GXA7	Arria-10 GX1150	Virtex-7 XC7V690T	Zynq XC7Z045	Zynq XC7Z020	Kintex-7 XC7K410T
Network	CNN	CNN	CNN	CNN	CNN	CNN	CNN	CNN	DCNN	CNN+DCNN
Frequency (MHz)	100	200	150	150	200	385	100	100	100	130
Precision	8-16 bit FT	32 bit FT	16 bit FX	8-16 bit FX	32 bit FT	16 bit FX	32 bit FT	16 bit FX	12 bit FX	16 bit FX
DSP Usage	256 (100%)	224 (88%)	780 (89%)	1,518 (100%)	224 (88%)	1,378 (91%)	784 (22%)	824 (92%)	220 (95%)	1,500 (97%)
Logic Usage	121K (52%)	200K (85%)	183K (84%)	161K (38%)	200K (85%)	-	118K (27%)	155K (71%)	25K (48%)	75K (30%)
On-chip RAM	1,552 (61%)	1,208 (64%)	486 (87%)	1,900 (70%)	1,208 (64%)	1,450 (53%)	703 (48%)	909 (82%)	67 (48%)	165 (21%)
Throughput (GOPS)	114.5	83.0	137.0	645.3	123.5	1790	162.1	229.5	2.6	$S_D=2$ 409.5
										$S_D=3$ 767
										$S_D=4$ 1,267.5
Power Efficiency (GOPS/W)	8.9	6.3	14.2	30.4	9.37	47.8	17.2	24.4	-	$S_D=2$ 92.7
										$S_D=3$ 173.5
										$S_D=4$ 286.8

access; the computation roof (CR) is the attainable performance. Therefore, in order to utilize all possible hardware resources and minimize the bandwidth in off-chip memory communications, we chose the optimal solution for each layer, as depicted in Fig. 13. Then, we performed cross-layer optimization [29]. We set the tiling parameters (T_m , T_n) for the FSRCNN and DCGAN to (56, 9) and (4, 128), respectively. Table VI shows the performance comparison of the existing method and the proposed methods. The experimental results show that the performance enhancement achieved by the proposed method is greater than the achieved by the existing methods for both the FSRCNN and the DCGAN.

First, DCGAN consists of four deconvolutional layers. Each layer has a greater number of input feature maps than output feature maps. Thus, T_m was set to 4, which was 42 times smaller than T_n . Our load balance-aware TDC method can improve performance even further when the resource underutilization problem exists in the conventional accelerators because $M \leq T_m$. The number of output feature maps in the last deconvolutional layer was smaller than T_m ; however, the speedup was not significant, because there was little difference between T_m and M . Since the resource underutilization problem was not apparent in the CLP of the DCGAN, the performance was improved only by the advantage of performing kernel computation in shorter cycles. Therefore, the proposed method was 3.59 times faster than the conventional method in the DCGAN.

Second, FSRCNN uses the deconvolutional layer as the last layer and can set the resolution of the output image according to S_D . Unlike in DCGAN, in FSRCNN 88.9% of the hardware resources are in the idle state, because the number of output feature maps M is nine times smaller than T_m . Thus, our load balance-aware TDC method could reduce the ratio of idle hardware to 55.5%, when the value of S_D was 2. Even when the value of S_D was 3, all the idle hardware was activated, resulting in a performance improvement of 81 times as compared to the conventional method. However, as shown in Table II, there are no zero-valued weights in the filters, and therefore, we could not take advantage of sparse matrix multiplication in this case.

However, Table II shows that the ratio of zero-valued weights is 43.8% when the value of S_D is 4. In other words, the load imbalance is serious, because the difference in the activated resources of the PEs is large. As a result, we evenly distributed the operations that the PEs executed unequally in conventional kernel computation. Therefore, our accelerator was able to run 108 times faster than the conventional accelerator using the same hardware resources.

B. Implementation Results of Proposed SR System

We evaluated our proposed DNN-based SR system using Vivado 2016.4. We designed our overall architecture with Verilog RTL. We set the working frequency of the FPGA as 130 MHz. In addition, our FPGA was connected to a 2880×1280 (QHD) panel.

Table VII shows a comparison of the implementation specifications of our accelerator with the various FPGA-based accelerators. We implemented QFSRCNN, which reduced the model size of the FSRCNN through the two-stage quantization algorithm. Since we quantized the model size to maximize the utilization of the DSP in the Kintex-7 410T FPGA, the DSPs were fully utilized. Additionally, BRAM usage was 21% of the total, with the advantage that the CNN model is smaller.

In conventional accelerators, the architecture is designed for either CNNs or DCNNs. However, the design of our accelerator is the first that has a hybrid form in which both CNNs and DCNNs are implemented together in the hardware platform. The throughput (GOPS) of each implemented accelerator, shown in the Table VII, was computed as the total computational complexity for spatial convolution divided by the average execution time per image. DCNNs increase the computational complexity in proportion to the power of S_D . For this reason, the rate of computational complexity occupied by the deconvolutional layer in QFSRCNN is 69.84%, 83.9%, and 90.26% when the value of S_D is 2, 3, and 4, respectively. However, our proposed DCNN accelerator could solve the loop dimension problem of the output image. Because we could simultaneously generate HR images with S_D^2 channels of LR

TABLE VIII
COMPARISON OF DIFFERENT SR SYSTEMS (FX: FIXED-POINT)

	[41] ANR	[42] SI	Proposed QFSRCNN
FPGA	Altera EP4S GX530	Kintex UltraScale XCKU040	Kintex-7 XC7K410T
Frequency (MHz)	136	150	130
Precision	FX	FX	16 bit FX
DSP Usage	-	108 (5.6%)	1500 (97%)
Logic Usage	-	3K (1.2%)	75K (30%)
Memory Size (Bytes)	235K	92K	329K
Power	-	-	4.42W
Implementation	FHD 60fps	UHD 60fps	QHD 141fps
Supported Scale	2X	2X	2X, 3X, 4X

images using the load balance-aware TDC method, $GOPS$ was higher in proportion to S_D .

A comparison of CNN accelerators for object detection and recognition showed that, the OpenCL-based method [22] had the highest throughput using the highest clock rate. However, when power consumption was considered, our on-chip memory-based accelerator had the highest power efficiency. In [21], the authors demonstrated that convolution computation can be performed in the frequency domain through fast Fourier transformation. Although their method had the advantage of less hardware resource usage in relation to performance, it required high power because it included a CPU together with off-chip memory. Another example of an accelerator, the state-of-the-art fusion architecture [19], reduced the amount of off-chip data transfer more than the conventional fusion architecture [18] by optimizing the dataflow between adjacent layers using more BRAMs. As a result, the amount of external memory access was reduced to improve power efficiency. However, a drawback remained in that power was still required for the off-chip memory. Without using off-chip memory, we enhanced power efficiency with an optimized dataflow for on-chip memory. Thus, our CNN accelerator is at least six times more power efficient than other hardware implementations.

Table VIII shows the hardware implementation results of our proposed system as compared to those of existing SR systems. Yang *et al.* [41] implemented anchored neighborhood

TABLE IX
IMAGE QUALITY COMPARISON OF VARIOUS METHODS

Test Sets	Scale	[41] ANR	[42] SI	[24] SRCNN	[25] SRCNN	[26] FSRCNN	Ours
Set5	2	33.83	34.78	36.34	36.66	37.00	36.20
Set14	2	29.77	31.63	32.18	32.45	32.63	32.03
B100	2	-	30.49	31.11	31.28	31.80	31.01
Set5	3	-	-	32.39	32.75	33.16	32.45
Set14	3	-	-	29.00	29.30	29.43	29.03
B100	3	-	-	28.20	28.35	28.52	28.20
Set5	4	-	-	30.09	30.49	30.71	30.09
Set14	4	-	-	27.20	27.50	27.59	27.22
B100	4	-	-	26.70	26.78	26.96	26.71

regression (ANR) in hardware to generate FHD images at 60fps, and Kim *et al.* [42] generated UHD images at 60 fps using the super-interpolation (SI) method. However, the scale factor supported by their methods was fixed to 2, and therefore, a limitation existed in that they could not generate an output image with a larger resolution image in the same hardware architecture. Our DNN-based SR system requires more hardware resources than conventional methods, but can support a variety of scale factors through the deconvolutional layer with the same hardware resources, because the convolutional layer transformed from the deconvolutional layer by the load balance-aware TDC method has the same kernel size, even if S_D is different. A virtual input/output (VIO) core [43] is a customizable core that allows virtual inputs and outputs to be added to our hardware description language (HDL) design. This core allows us to drive internal FPGA signals synchronously or asynchronously. The FSRCNN is characterized by the fact that the weights of the convolutional layers do not change even if the scale factor changes, but only the weights of the deconvolutional layer [26]. We pre-stored the weights of all the deconvolutional layers, each 1.6KB in size, in ROM to use the VIO core. Therefore, we could obtain the output by adjusting the internal signals through the VIO core without having to re-synthesize to change the weights of the deconvolutional layer stored in the ROM when different scale factors were needed.

Table VIII also shows that our system can generate QHD at 141 fps when the scale factor is 2. In the case where a UHD video stream was required, our system could generate UHD images at 62.7 fps using approximately twice the number of BRAMs. When the scale factor is greater than 2, the speed of our system is inversely proportional to the input resolution. For example, if the scale factor is 3, an image with a resolution of 1280×720 , which is smaller than the FHD, is used as the input to generate the UHD image.

Fig. 14 demonstrates our DNN-based SR system. We confirmed that HR images can be generated from the QHD panel for mobile applications. Table IX shows a comparison in terms of image quality of various SR methods in different scale factors. We evaluated the performance of the SR systems and algorithms on the datasets that are most frequently used. Although our system had a lower PSNR than the FSRCNN because of the two-stage quantization method for high power efficiency and hardware implementation, our method could

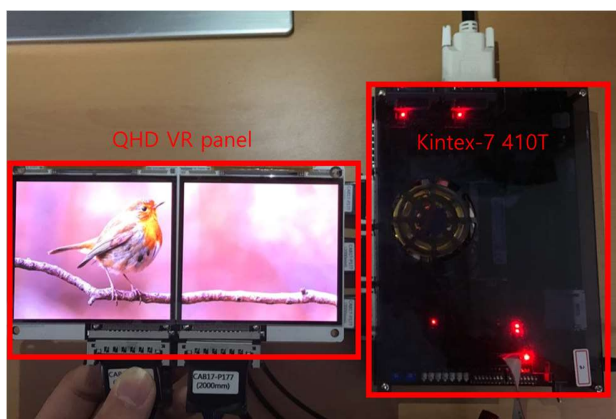


Fig. 14. Demonstration of the DNN-based super-resolution system.

achieve higher image quality than existing systems.

VII. CONCLUSION

In this paper, we proposed an energy-efficient DNN based SR architecture for hardware implementation. First, we presented a novel methodology to optimize the dataflow for effectively designing the DCNN with higher computational complexity than the CNN in hardware implementation. In addition, we proposed an on-chip memory-based DNN architecture for high energy-efficiency. Our experimental results showed that our DCNN accelerator can achieve a speed up to 108 times faster than a conventional DCNN accelerator with the same hardware resources. Moreover, the proposed SR architecture was shown to be at least six times more power efficient than the state-of-the-art implementations.

REFERENCES

- [1] R. Girshick, J. Donahue, T. Darrell, and J. Malik, "Rich feature hierarchies for accurate object detection and semantic segmentation," in *Proc. IEEE CVPR*, Jun. 2014, pp. 580-587.
- [2] T. He, W. Huang, Y. Qiao, and J. Yao, "Text-attentional convolutional neural network for scene text detection," *IEEE Trans. Image Process.*, vol. 25, no. 6, pp. 2529-2541, Jun. 2016.
- [3] P. Sermanet, D. Eigen, X. Zhang, M. Mathieu, R. Fergus, and Y. LeCun, "OverFeat: Integrated recognition, localization and detection using convolutional networks," [Online]. Available: <https://arxiv.org/abs/1312.6229>
- [4] A. Krizhevsky, I. Sutskever, and G. E. Hinton, "ImageNet classification with deep convolutional neural networks," in *Proc. NIPS*, 2012, pp. 1097-1105.
- [5] K. Simonyan and A. Zisserman, "Very deep convolutional networks for large-scale image recognition," [Online]. Available: <https://arxiv.org/abs/1409.1556>
- [6] K. He, X. Zhang, S. Ren, and J. Sun, "Deep residual learning for image recognition," in *Proc. IEEE CVPR*, Jun. 2016, pp. 770-778.
- [7] R. Collober and J. Weston, "A unified architecture for natural language processing: Deep neural networks with multitask learning," in *Proc. ICML*, 2008, pp. 160-167.
- [8] R. Zhao, X. Niu, Y. Wu, W. Luk, and Q. Liu, "Optimizing cnn-based object detection algorithms on embedded fpga platforms," in *Proc. Appl. Reconf. Comput.*, 2017, pp. 255-267.
- [9] T. Chen, Z. Du, N. Sun, J. Wang, C. Wu, Y. Chen, and O. Temam, "Diannao: A small-footprint high-throughput accelerator for ubiquitous machine-learning," in *Proc. ACM SIGPLAN*, 2014, pp. 269-284.
- [10] C. Zhang, P. Li, G. Sun, Y. Guan, B. Xiao, and J. Cong, "Optimizing fpga-based accelerator design for deep convolutional neural networks," in *Proc. FPGA*, 2015, pp. 161-170.
- [11] H. Li, X. Fan, L. Jiao, W. Cao, X. Zhou, and L. Wang, "A high performance FPGA-based accelerator for large-scale convolutional neural networks," in *Proc. FPL*, 2016.
- [12] Y. Ma, N. Suda, Y. Cao, J.-S. Seo, and S. Vrudhula, "Scalable and modularized rtl compilation of convolutional neural networks onto FPGA," in *Proc. FPL*, 2016.
- [13] J. Qiu, J. Wang, S. Yao, K. Guo, B. Li, E. Zhou, J. Yu, T. Tang, N. Xu, S. Song, Y. Wang, and H. Yang, "Going deeper with embedded fpga platform for convolutional neural network," in *Proc. FPGA*, 2016, pp. 26-35.
- [14] M. Motamedi, P. Gysel, V. Akella, and S. Ghiasi, "Design space exploration of fpga-based deep convolutional neural networks," in *Proc. ASP-DAC*, 2016, pp. 575-580.
- [15] Y. Shen, M. Ferdman, and P. Milder, "Overcoming resource under-utilization in spatial CNN accelerators," in *Proc. FPL*, 2016, pp. 1-4.
- [16] Y. Shen, M. Ferdman, and P. Milder, "Maximizing CNN accelerator efficiency through resource partitioning," in *Proc. ISCA*, 2017.
- [17] Y. Ma, Y. Cao, S. Vrudhula, and Jae-sun Seo, "Optimizing loop operation and dataflow in fpga acceleration of deep convolutional neural networks," in *Proc. FPGA*, 2017, pp. 45-54.
- [18] M. Alwani, H. Chen, M. Ferdman, and P. Milder, "Fused-layer CNN accelerators," in *Proc. MICRO*, 2016, pp. 1-12.
- [19] Q. Xiao, Y. Liang, L. Lu, S. Yan, and Y.-W. Tai, "Exploring heterogeneous algorithms for accelerating deep convolutional neural networks on fpgas," in *Proc. DAC*, 2017, pp. 1-6.
- [20] H. Yonekawa and H. Nakahara, "On-chip memory based binarized convolutional deep neural networks applying batch normalization free technique on an fpga," in *Proc. IPDPSW*, 2017, pp. 98-105.
- [21] C. Zhang and V. Prasanna, "Frequency domain acceleration of convolutional neural networks on cpu-fpga shared memory system," in *Proc. FPGA*, 2017, pp. 35-44.
- [22] J. Zhang and J. Li, "Improving the performance of opencl-based fpga accelerator for convolutional neural networks," in *Proc. FPGA 2017*, pp. 25-34.
- [23] Y.-H. Chen, T. Krishna, J. S. Emer, and V. Sze, "Eyeriss: An energy-efficient reconfigurable accelerator for deep convolutional neural networks," in *IEEE Int. Solid-State Circuits Conf. (ISSCC) Dig. Tech. Paper*, Jan./Feb. 2016, pp. 262-263.
- [24] C. Dong, C. C. Loy, K. He, and X. Tang, "Learning a deep convolutional neural network for image super-resolution," in *Proc. ECCV*, 2014, pp. 184-199.
- [25] C. Dong, C. C. Loy, K. He, and X. Tang, "Image super-resolution using deep convolutional networks," *IEEE Trans. Pattern Anal. Mach. Intell.*, vol. 38, no. 2, pp. 295-307, Feb. 2015.
- [26] C. Dong, C. C. Loy, and X. Tang, "Accelerating the super-resolution convolutional neural network," in *Proc. ECCV*, 2016, 391-407.
- [27] M. D. Zeiler, D. Krishnan, G. W. Taylor, and R. Fergus, "Deconvolutional networks," in *Proc. CVPR*, 2010, pp. 2528-2535.
- [28] X. Zhang, S. Das, O. Neopane, and K. Kreutz-Delgado, "A design methodology for efficient implementation of deconvolutional neural networks on an fpga," [Online]. Available: <https://arxiv.org/abs/1705.02583>
- [29] J.-W. Chang and S.-J. Kang, "Optimizing fpga-based convolutional neural networks accelerator for image super-resolution," in *Proc. ASP-DAC*, 2018, pp. 343-348.
- [30] M. D. Zeiler and R. Fergus, "Visualizing and understanding convolutional networks," in *Proc. ECCV*, 2014, pp. 818-833.
- [31] X. Glorot, A. Bordes, and Y. Bengio, "Deep sparse rectifier neural networks," in *Proc. AISTATS*, 2011, p. 275.
- [32] K. He, X. Zhang, S. Ren, and J. Sun, "Delving deep into rectifiers: surpassing human-level performance on imagenet classification," in *Proc. ICCV*, 2015, 1026-1034.
- [33] Xilinx, 7 series FPGAs memory resources user guide.
- [34] M. Courbariaux, Y. Bengio, and J. David, "Low precision arithmetic for deep learning," [Online]. Available: <https://arxiv.org/abs/1412.7024>
- [35] D. Lin, S. Talathi, and S. Annapureddy, "Fixed point quantization of deep convolutional networks," in *Proc. ICML*, 2016, 2849-2858.
- [36] Y. Jia, E. Shelhamer, J. Donahue, S. Karayev, J. Long, R. Girshick, S. Guadarrama, and T. Darrell, "Caffe: Convolutional architecture for fast feature embedding," [Online]. Available: <https://arxiv.org/abs/1408.5093>
- [37] ITU-R Recommendation BT.601-5: Studio encoding parameters of digital television for standard 4:3 and wide-screen 16:9 aspect ratios
- [38] Y. Yang, P. Yuhua, and L. Zhaoguang, "A fast algorithm for YCbCr to RGB conversion," *IEEE Trans. Consumer and Electronics*, vol. 53, no. 4, Nov. 2007.
- [39] A. Radford, L. Metz, and S. Chintala, "Unsupervised representation learning with deep convolutional generative adversarial networks," [Online]. Available: <https://arxiv.org/abs/1511.06434>
- [40] S. Williams, W. Andrew, and D. Patterson, "Roofline: an insightful visual performance model for multicore architectures," *Communications of the ACM*, vol. 52, no. 4, Apr. 2009.
- [41] M.-C. Yang, K.-L. Liu, and S.-Y. Chien, "A Real-time fhd learning-based super-resolution system without a frame buffer," *IEEE Trans. Circuits Syst. II Exp. Briefs*, vol. 64, no. 12, pp. 1407-1411, Dec. 2017.
- [42] Y. Kim, J.-S. Choi, and M. Kim, "2X super-resolution hardware using edge-orientation-based linear mapping for real-time 4k uhd 60 fps video applications," *IEEE Trans. Circuits Syst. II Exp. Briefs*, 2018.
- [43] Xilinx, Chipscope pro software and cores user guide.